npj | climate and atmospheric science

www.nature.com/npjclimatsci

ARTICLE OPEN

Check for updates

Impact of satellite thickness data assimilation on bias reduction in Arctic sea ice concentration

Jeong-Gil Lee[1] and Yoo-Geun Ham[1]✉

The impact of assimilating satellite-retrieved Arctic sea ice thickness (SIT) on simulating sea ice concentration (SIC) climatology in CICE5 is examined using a data assimilation (DA) system based on the ensemble optimal interpolation. The DA of the SIT satellite data of CryoSat-2 and SMOS during 2011–2019 significantly reduces the climatological bias of SIC and SIT in both sea ice melting and growing seasons. Moreover, the response of SIC to SIT change is strongly dependent on the seasons and latitudinal locations. The SIT in the inner ice zone thickens due to the SIT DA during the boreal winter wherein the SIT observation is available; the ice melting throughout the subsequent seasons is attenuated to increase SIC during the boreal summer to reduce the simultaneous SIC bias. In marginal ice zones, the positive SIT bias depicted in the control simulation is significantly reduced by SIT DA, which reduces the positive SIC bias. The idealized experiments of reducing the SIT show that the enhanced ice bottom melting process plays a crucial role in reducing the SIC; the prescribed SIT thinning increases the ice bulk salinity due to the weak gravity drainage of brine and increases the ice bulk temperature due to the decrease of the sea ice albedo. The augmentation of the ice salinity and temperature contributes to the shrinkage of the ice enthalpy, boosting the bottom melting process, which leads to SIC decrease.

npj Climate and Atmospheric Science (2023)6:73 ; https://doi.org/10.1038/s41612-023-00402-6

INTRODUCTION

Arctic sea ice is rapidly and consistently declining due to anthropogenic forcing[1–4]. Moreover, drastic changes in the Arctic sea ice conditions lead to the amplification of the interannual sea ice variability, which means that the accurate prediction of Arctic sea ice extent (SIE) is more challenging in warm climates[5–7].

The interannual variations in the amount of Arctic sea ice substantially affect the Arctic ecosystem and Arctic shipping route (i.e., Northern Sea Route) for commercial shipments[8,9]. Additionally, they potentially impact the mid- and low-latitude weather and climate system via the atmospheric teleconnection processes[10–13]. Thus, the demands for the accurate prediction of the Arctic sea ice amount at interannual time scales have been augmented in recent decades[14].

The accurate predictions of the sea ice amount using dynamical models depend on the quality of the initial conditions[15,16], which can be obtained by implementing data assimilation (DA) techniques using available sea ice observations[17,18]. As a representative prognostic variable of the dynamical sea ice model, sea ice concentration (SIC) has been assimilated to produce a reanalysis for several decades[17,19–22]. However, the impact of SIC DA hardly lasts for more than a season as SIC represents the surface sea ice condition, which is strongly affected by atmospheric variables with the time scale of a few days[23]. Instead, sea ice thickness (SIT) is expected to be more sustainable than SIC; therefore, the assimilation of SIT will afford higher predictability than that of SIC[24].

The satellite-based Arctic SIT observations have been produced since the early 2000s[25], although retrieval methods are in an early stage of development. Until the early 2010s, low-resolution spatiotemporal data for Arctic SIT was available, and SIT was updated using SIC observations through multivariate DA frameworks[21,26]. Although the simulation quality of the assimilated SIT climatology is good, this methodology has limitations as the SIT updates are dependent on the modeled relationship between SIC and SIT. This is expected to lead to inconsistencies between the updates and observations in some cases; SIT updates using the multivariate DA framework can increase the SIT bias. In this regard, the direct injection of the SIT observation into a numerical model using a DA scheme is clearly required to produce realistic SIT initial conditions.

Fortunately, the accumulation of satellite-based SIT observations from over more than a decade provides an opportunity for initializing SIT by directly injecting the SIT observations[27,28]. Recent studies have tried to initialize SIT by assimilating satellite-derived CryoSat-2[29] (CS2) and/or Soil Moisture Ocean Salinity[30] (SMOS) data[31–36]. It is shown that the SIT bias reduces by about 20% when the merged CS2 and SMOS data are assimilated into the coupled ocean and sea ice model of the TOPAZ4 system[37,38]. The assimilation of CS2 data into the Met Office's coupled seasonal prediction system (GloSea) leads to the correction of the negative SIT biases in the central Arctic region during the boreal winter[32]. Similarly, it is demonstrated that the underestimated SIT represented in the Met Office's Forecast Ocean Assimilation Model (FOAM) without any addition of the SIT data is effectively thickened by the addition of CS2 data[34]. Interestingly, the DA of SIT leads to better simulations in not only the assimilated observation (i.e., SIT) but also the SIC[39–42]. Similarly, the benefits of assimilating CS2 SIT observations on the seasonal forecast of Arctic SIE during the boreal autumn season have been presented[32]. While the assimilation of the CS2 SIT data leads to the improvement in simulating Arctic SIE via the modulation of the thick sea ice amount, the assimilation of thin sea ice using the SMOS observation significantly impacts SIC in marginal ice zones (MIZs) has been demonstrated[43]. This denotes the complementarity between the CS2 and SMOS SIT data. Therefore, the SIT DA using both satellites would further improve the simulation quality of the Arctic sea ice[35,42,44].

Furthermore, the constructive effect on the short-term operational SIC forecasts has been demonstrated using the satellite SIT

[1]Department of Oceanography, Chonnam National University, Gwangju 61186, South Korea. ✉email: ygham@jnu.ac.kr

data of the CS2 and SMOS merged data[37] or individual CS2 and SMOS data[35,45]. It has been found that the quality of mean SIT and the short-term forecasting skills for SIC are improved when assimilating CS2 data into FOAM during the boreal summer and winter seasons[33].

The positive impact of the SIT DA on SIC simulation and forecast has often been reported; however, few studies have explored the detailed physical mechanism of how the SIT increment modulates SIC. The thinning of sea ice, which weakens the role of SIT as an insulating cap of the atmosphere-ocean interfaces, is causative of the additional release of heat from the warmer ocean to the colder atmosphere during the winter season (so-called "insulation effect")[46,47]. Consequently, locally increased surface warming led by thinner sea ice would further boost the thinning of ice and lead to Arctic amplification due to the potential positive feedback[48]. However, except for the insulation effect, the detailed mechanism of the indirect impact of SIT on SIC variation is still not well known. In other words, although the realistic SIT states are known to affect the accurate estimation of the growth/melting rate of the sea ice and the resultant sea ice opening/closing modulating the ocean-atmosphere interactions[49–51], its detailed process is still unknown.

In this study, the Arctic sea ice for a decade (i.e., 2011–2019) is reanalyzed by assimilating satellite-based SIT into the Community Ice CodE version 5.1.2 (CICE5) using the ensemble optimal interpolation (EnOI) scheme[52–54], and the indirect response of SIC led by SIT observation is examined. To understand the detailed process of how the SIT observations improve the simulation quality of SIC, idealized experiments and heat budget analysis are performed.

RESULTS

Impact of the sea ice thickness data assimilation on sea ice simulation

Fig. 1 displays the monthly averaged Arctic SIE, defined as the cumulative area of all grid cells with SIC greater than 0.15 over the Northern Hemisphere during 2011–2019. The simulated SIE in the experiment without DA (referred to as noDA hereinafter) tends to be overestimated during the boreal winter season from December to March compared to the satellite SIC data. For example, the SIE during the boreal winter of 2011/12 is over 15 $\times 10^6$ km^2 in noDA, while the satellite-retrieved value is between 13 and 14 $\times 10^6$ km^2. In contrast, the simulated SIE in noDA is systematically underestimated from August to September (AS) compared to the satellite observations. Particularly, the SIE during the boreal summer of 2012 in noDA is only half of that observed. Consequently, the climatological bias of SIE in noDA exhibits positive and negative values during the boreal winter and boreal summer/autumn, respectively (Fig. 1b).

The assimilation of the SIT satellite observation systematically reduces the SIE bias. This improvement is particularly evident after 2014. For example, during the boreal winter of 2013/14, the overestimation of SIE in noDA is not apparent in the SIT assimilated experiment (referred to as DA hereinafter). This bias correction is well demonstrated in the climatological SIE time series (Fig. 1b), which denotes that the positive SIE bias from December–February (DJF) is systematically reduced in DA.

Note that although the SIT observation is assimilated only in the boreal winter season (i.e., from October to April), the SIE bias also substantially reduces during the boreal summer/autumn season, where the SIT observation is not directly assimilated. For example, the climatological SIE bias during the AS season is -1.7×10^6 km^2 in noDA, which tends to be nearly zero in DA (Fig. 1b). This implies that the assimilation of the satellite SIT observation improves the simulation quality of SIC during not only the season in which the observation is assimilated but also the remaining seasons. This might possibly be due to the multi-season persistency of the sea ice states, as previously reported[23,55].

The climatological response of SIC by the SIT DA is examined using the satellite observation data (i.e., SSMIS CDR) for the DJF season in Fig. 2. In noDA, the weak positive SIT bias is evident in the Barents and Greenland Seas and the Sea of Okhotsk, while the negative SIT bias is robust in inner ice zone (IIZ) (Fig. 2a). By assimilating the SIT observations, the climatological SIT becomes thinner in MIZ, particularly over the Barents-Kara Sea and the Sea of Okhotsk, and becomes thicker in IIZ (Fig. 2b). The mean SIT in MIZ is generally thinner for DA compared to noDA, and a similar result appears in the Sea of the Okhotsk and the Barents Seas (Fig. 2e). Therefore, in DA, both the positive SIT bias in MIZ and the negative SIT bias in IIZ are reduced.

In noDA, the positive SIC bias is prominent in MIZ, while the bias amplitude is relatively weak in IIZ (Fig. 2c). The reason for the weak Arctic SIC bias amplitude in IIZ is that those areas are fully covered by sea ice during the boreal winter season in both simulations and observations. Interestingly, the thinning of SIT in DA contributes to the reduction of SIC in MIZ where the positive SIT bias is reduced (Fig. 2d–f). In addition, the reduction in SIT due to DA leads to a decrease in sea ice area (SIA) in MIZ. This reduction in SIC contributes to weakening the SIC bias in noDA.

While the climatological SIT changes due to the SIT DA in MIZ mainly modulates the SIC during the boreal winter season, the SIT changes in IIZ play a positive role in modulating the SIC climatology mainly during the sea ice melting season (i.e., the AS season) (Fig. 3). The strong negative bias for both SIC and SIT in noDA is distributed over the northern Greenland and CAP regions in IIZ, while the bias in MIZ is faint as the sea ice is nearly melted in both

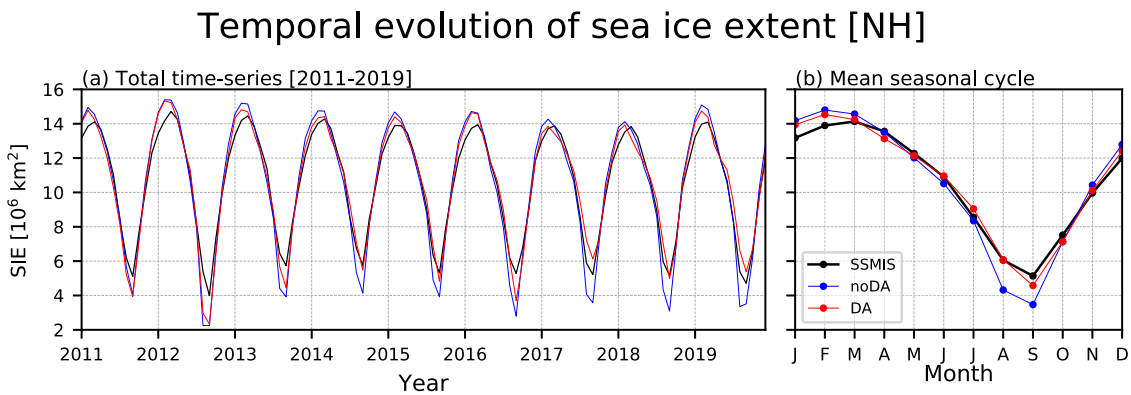

Fig. 1 Time-series of Arctic sea ice extent during 2011–2019. The temporal evolution (**a**) and mean seasonal cycle (**b**) of the Northern Hemisphere sea ice extent index (**10^6 km^2**) during 2011–2019 for the SSMIS CDR satellite data (black), noDA experiment (blue), and DA experiment (red).

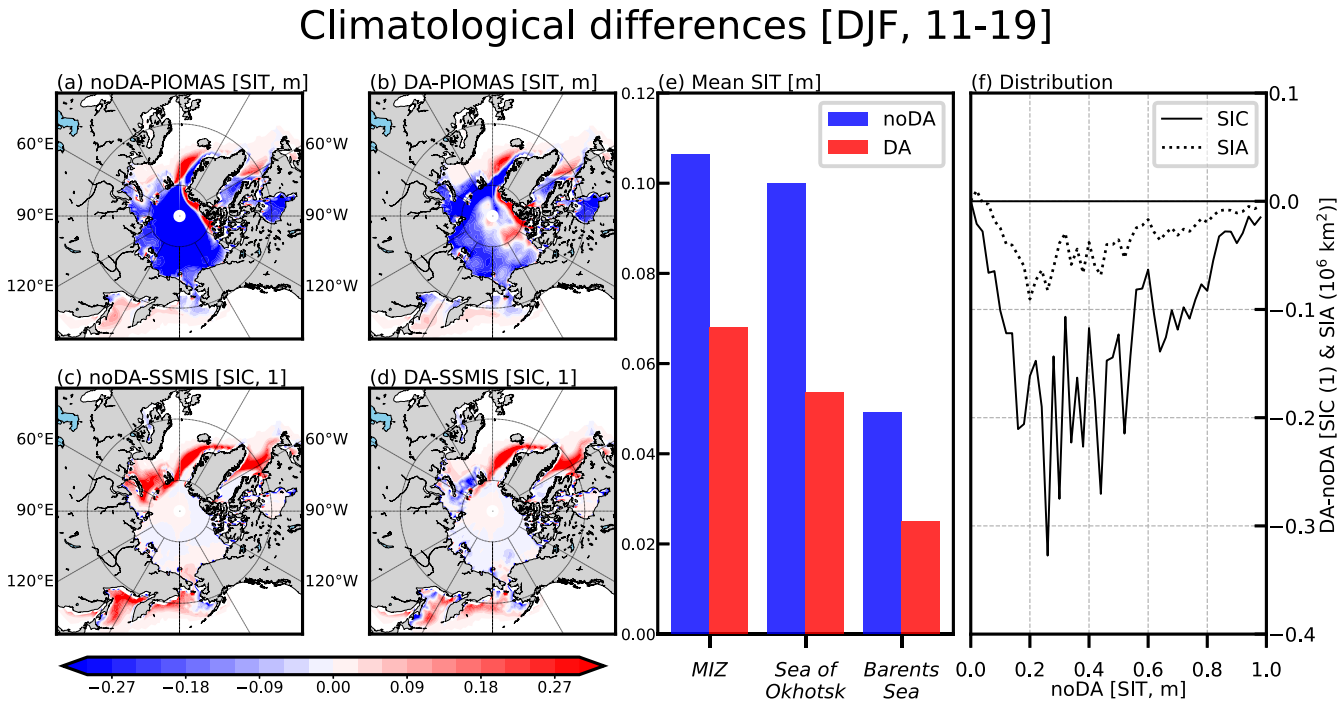

Fig. 2 Mean bias of simulated winter SIT and SIC during 2011–2019. Climatological bias of the SIT (m) in noDA (**a**) and DA (**b**) with respect to PIOMAS and of SIC (a fraction from 0 to 1) in noDA (**c**) and DA (**d**) with respect to SSMIS CDR during the DJF season over 2011–2019. Climatological average of the SIT in noDA (blue) and DA (red) for MIZ where the SIT in noDA is thinner than 0.4 m, the Sea of Okhotsk (140 − 160°E, 40 − 60°N), and the Barents Sea (30 − 60°E, 70 − 75°N) (**e**). The differences of SIC (solid) and SIA (dotted) between DA and noDA experiments are distributed as a function of SIT in noDA (**f**).

the simulations and observations during this season (Fig. 3a–c). The polar-region-averaged (poleward of 60°N) SIC in noDA is systematically underestimated by more than 0.25 compared to the SSMIS CDR satellite data. Note that the spatial distribution of the SIT bias during the AS season is almost identical to that during the DJF season, indicating that the spatial distribution of the SIT bias remains similar for all seasons.

In most IIZ, both SIT and SIC in DA are overall higher compared to those in noDA (Fig. 3b–d). As the direct injection of the satellite observations through DA is performed only during the boreal winter season, the thickened SIT in DA during the AS season is induced by the indirect impact of DA; Fig. 4 showed the differences in sea ice mass (SIM) and SIC over the inner ice zone adjacent to Fram Strait (IIZ-FS) and sea ice volume flux (SIVF) over the Fram Strait region (FS) between DA and noDA. The Fram Strait serves as the primary outlet for the export of sea ice from the Arctic. It shows that the SIC in DA increases in the summer months along with the increase in SIM throughout the year (blue and red lines in Fig. 4). The thickened SIT during the boreal winter season in DA prevents the sea ice from melting during the following summer seasons, and thus, the significant negative SIE bias disappears (Figs. 1b and 3d); the thickened SIT during the boreal winter season is sustained for multi seasons as shown by the increase in SIM[23,56]. Indeed, the climatological mean SIC tendency by thermodynamic process during the melt season (i.e., April–August) in DA (-0.14% day^{-1}) is approximately half that in noDA (-0.32% day^{-1}), where the difference in the dynamic process is not evident over the central Arctic region (poleward of 80°N).

In addition to this, we found that the sea ice volume flux (*SIVF*) through the FS region also contributes to an increase in SIC with increase in SIM over IIZ-FS (black solid line in Fig. 4). The *SIVF* is calculated by

$$SIVF = \sqrt{SIVF_z^2 + SIVF_m^2} \quad (1)$$

where $SIVF_z$ ($SIVF_m$) is the sea ice drift for the zonal (meridional) component. The zonal (or meridional) volume flux $SIVF_z$ (or $SIVF_m$) for the Fram Strait is the integral of volume flux across each grid cell ($i = 1, \ldots, n$) located at the boundary and is calculated by

$$SIVF_{z\,or\,m} = \sum_{i=1}^{n} I_i G D_i c_i \quad (2)$$

where D_i is the zonal or meridional component of the sea ice drift at the grid cell numbered as i, G is the length of the grid cell c_i is SIC, and I_i is SIT of the cell[57]. The sea ice variables used for calculation are based on monthly data. This could be attributed to the thicker SIT in DA compared to noDA, which increases the mass of sea ice, thereby reducing its sensitivity to wind and ocean current stresses. Consequently, the flow velocity of sea ice is reduced, which in turn mitigates sea ice export. This suggests that the increase in summer SIC over the IIZ region may be partly attributable to the consistent impact of the dynamic component.

On the other hand, the simultaneous impact of thinner sea ice in MIZ on the decrease of the SIC climatology during the boreal winter is also needed to be investigated. The following subsection demonstrates the primary mechanism responsible for the reduction in the SIC climatology due to the thinning of the SIT climatology in MIZ during the boreal winter season.

Physical mechanism of the SIC reduction due to the SIT thinning

To explore the detailed mechanism of how the given SIT reduction decreases the SIC in MIZ during the boreal winter, idealized experiments are conducted assuming that each category of SIT is reduced by 0.05m over the region where SIT<0.4m (referred to as "EXP") compared to the control simulation (which is identical to noDA; referred to as "CTL" in this subsection). Note that the SIT initial conditions in EXP are constrained not to be smaller than zero to maintain the physical boundaries; if the updated SIT in EXP

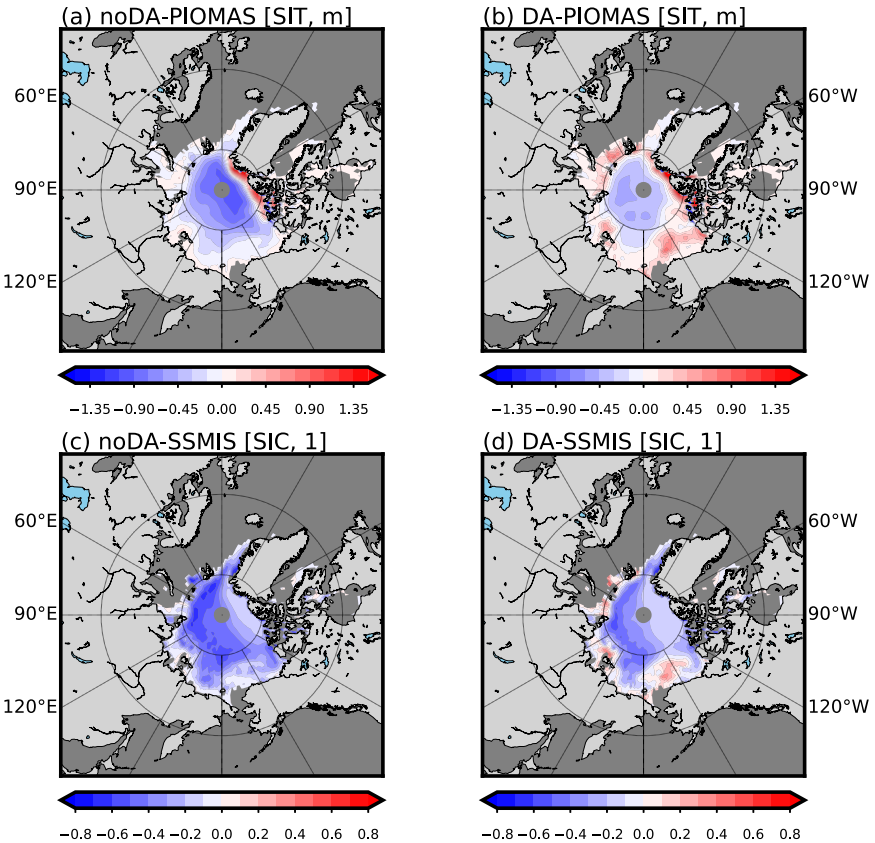

Fig. 3 Mean bias of simulated summer SIT and SIC during 2011–2019. Climatological bias of the SIT (m) in noDA (**a**) and DA (**b**) with respect to PIOMAS and of SIC (a fraction from 0 to 1) in noDA (**c**) and DA (**d**) with respect to SSMIS CDR during the AS season over 2011–2019.

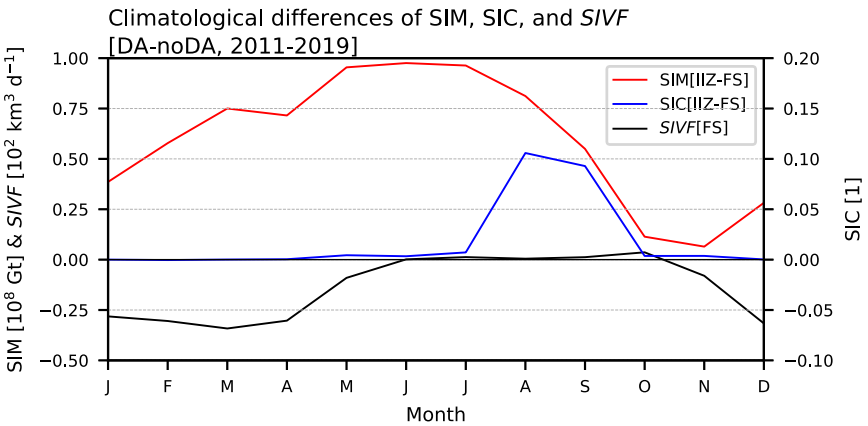

Fig. 4 Changes in SIM, SIC, and *SIVF* led by SIT data assimilation. The climatological differences of sea ice mass (SIM, red line, over the Central Arctic region (IIZ-FS), 20°W-0°E, 80°N-90°N), SIC (blue line, over the IIZ-FS), and the sea ice volume flux (***SIVF***, black, over the Fram Strait (FS) region, 20°W-0°E, 75°N-80°N) during 2011–2019.

is less than zero, a small value (i.e., 10^{-9}cm) is prescribed as the initial condition. To objectively explore the impact of SIT reduction, none of the variables except for SIT was changed in the initial conditions. To reduce the noise in the results induced by the small number of samples, EXP and CTL are performed using the initial conditions on December 1st from 2000 to 2019 (a total of 20 ensemble members). Twenty simulation-averaged values are presented as the final results.

Note that the differences between EXP and CTL are solely originated from the SIT differences in the initial conditions, and identical atmospheric and ocean boundary conditions in both EXP and CTL reduces the impact of the SIC due to the initial SIT

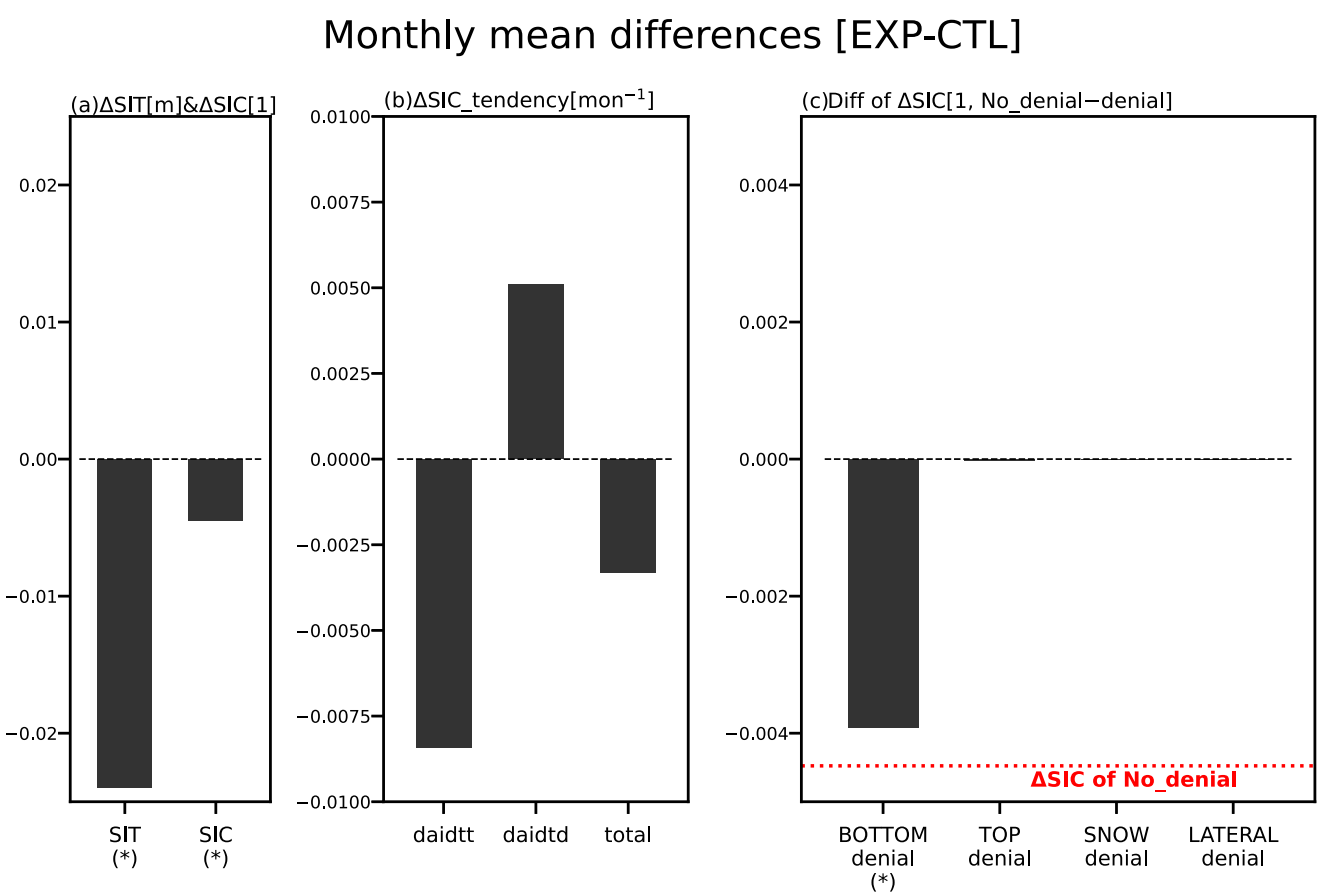

Fig. 5 Investigation for the impact of SIT reduction and related mechanism through the idealized experiments. The monthly (December) area-averaged mean differences between EXP and CTL in MIZ during 2000–2019 for SIT (m) and SIC (a fraction from 0 to 1) (**a**) and tendency terms of SIC (**b**). The daidtt and daidtd are the tendency terms of SIC due to the thermodynamic and dynamic processes (**a** fraction from 0 to 1 per month), respectively. The symbol "Δ" represents the differences between the SIT reduction experiment and the control experiment (i.e., EXPs minus CTLs). Each difference of ΔSIC between denial experiments and No_denial is calculated (**c**). The red-dotted line in (**c**) represents the ΔSIC of No_denial, which is the same as the 2nd bar in (**a**). The area average is calculated only for the regions where SIC is reduced by thinning ice (i.e., ΔSIC of No_denial is negative). The asterisk signs on the labels of x-axis denote a statistically significant difference between EXP and CTL (p-value < 0.01).

thinning. Based on the e-folding time of the initial SIC responses (not shown), we calculated 1-month-averaged differences between two experiments. In addition, we only analyzed regions where the SIT in CTL was thicker than 0.05m to avoid the arbitrary effect of the constraint condition (i.e., 10^{-9}cm).

Fig. 5a displays the MIZ-averaged monthly differences between EXP and CTL for the prognostic sea ice variables (ΔSIC and ΔSIT). In EXP, the reduction of SIT in MIZ is clearly shown as designed, even though its amplitude is smaller than the initial prescribed differences due to the identical atmospheric and oceanic boundary forcings. Interestingly, as a response to the negative ΔSIT, SIC tends to be reduced in the entire MIZ (i.e., negative ΔSIC) (Fig. 5a), which is consistent with the results in the SIT DA. Both reductions in SIT and SIC are statistically significant by performing the two-tailed Student's t-test. To investigate the cause of SIC reduction led by the thinning of SIT in MIZ, the differences in the monthly-averaged SIC tendency terms due to dynamics/transport (daidtd) and due to thermodynamics (daidtt) provided by CICE model output between EXP and CTL are calculated (Fig. 5b). Clearly, the tendency due to the thermodynamic processes is the main factor causing the total SIC tendency change between EXP and CTL, while the tendency in the dynamical/transport process exhibited weak positive values. The effect caused by the dynamical process is thought to be a response to the changes led by the thermodynamical process, because if the SIC decreased due to thermodynamics (i.e., daidtt <0), dynamically driven changes in SIC would contribute to an increase (i.e., daidtd >0) by reducing the possibility of dynamical sea ice breaking[58,59]. This means that the thermodynamic processes mainly lead to the intensification of the dwindling of SIC in EXP.

To further reveal the thermodynamic process responsible for the SIC reduction, mechanism-denial experiments are conducted. That is, while performing EXP and CTL, one of the thermodynamic mechanisms is removed to identify the fundamental process in the response of SIC to SIT reduction. The denial experiments are conducted by removing either ice melt on the bottom (EXP/CTL_bottom), ice melt on top (EXP/CTL_top), ice melt at the snow boundary surface (EXP/CTL_snow), or the lateral ice melting processes (EXP/CTL_lateral). The difference between two denial experiments (e.g., the difference between EXP_bottom and CTL_bottom) is compared to the difference between EXP and CTL to quantify the role of the thermodynamic processes on SIC reduction. The difference between EXP and CTL is referred to as "No_denial" hereinafter, and the differences in SIC between EXPs and CTLs by removing the ice melt on the bottom, ice melt on top, ice melt at the snow boundary surface, and ice melt on lateral directions are referred to as BOTTOM_denial, TOP_denial, SNOW_denial, and LATERAL_denial, respectively.

The differences in ΔSIC between any denial experiment and No_denial are shown in Fig. 5c. Through a series of denial experiments, the sea ice bottom melting is determined to be the primary factor in decreasing SIC by a given SIT reduction. The

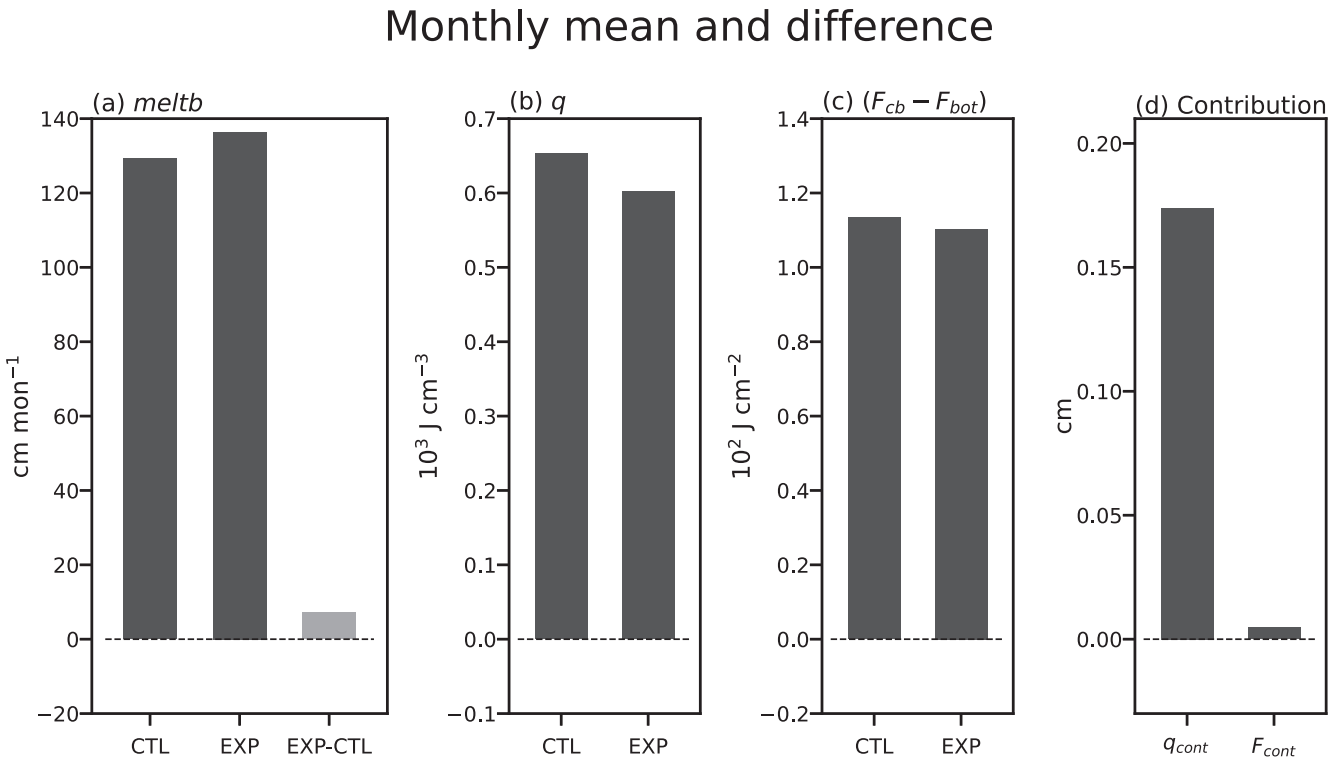

Fig. 6 Changes in ice bottom melting (*meltb*) and related variables induced by SIT reduction. The monthly (December) area-averaged mean of CTL (1st black bars) and EXP (2nd black bars) and their differences (3rd gray bars) in MIZ for the ice bottom melting (**a**), ice enthalpy (**b**), and heat balance term (**c**), and the quantified contribution of enthalpy and heat balance by scaling to same unit (**d**) during 2000–2019. The area average is calculated only for the regions where SIC is reduced by thinning ice (i.e., ΔSIC of No_denial is negative).

degree of SIC reduction by a given SIT thinning in TOP_denial, SNOW_denial, and LATERAL_denial is similar to that for No_denial; therefore, the difference in ΔSIC from No_denial and the above denial experiments is nearly zero. This implies that the corresponding mechanisms are not responsible for the SIC reduction in No_denial. In contrast, in BOTTOM_denial, the SIC decreases because the SIT thinning in No_denial almost disappears (1st bar in Fig. 5c). This clearly indicates that the enhanced sea ice bottom melting process is key process leading the SIC reduction according to the prescribed SIT thinning.

The amplitude of the ice bottom melting (referred to as *meltb*, unit of cm day^{-1}) is determined as follows:

$$meltb = \frac{F_{cb} - F_{bot}}{q} \tag{3}$$

where q is the positive of the enthalpy of the bottom ice layer (W day cm^{-3}), denoting the energy needed to melt a unit volume of sea ice[60]. F_{cb} is the downward conductive heat flux from the ice top to the ice bottom surface (W cm^{-2}), and F_{bot} is the downward heat flux from the ice to the ocean (W cm^{-2}). If F_{cb} (F_{bot}) is negative, the flux is transferred from the ice bottom to the top surface (from the ocean to the ice). In other words, if F_{cb}>F_{bot} (i.e., the transfer of the energy to the upper sea ice is lower than the input of the energy from the sea ice bottom), ice melting occurs at the bottom surface ($meltb$>0). The ice bottom melting increases (i.e., increase in *meltb*) when the input of the heat flux increases (i.e., increase in $F_{cb} - F_{bot}$) and/or the energy needed to melt decreases (i.e., decrease in q).

Fig. 6 displays the MIZ-averaged monthly-mean of *meltb*, the ice enthalpy of the bottom ice layer (q), and the net transfer of the energy ($F_{cb} - F_{bot}$) in EXP and CTL, and the contribution of q and $F_{cb} - F_{bot}$ on the change in *meltb*. The *meltb* in EXP is amplified more than that in CTL (Fig. 6a) with the reduction in the enthalpy (Fig. 6b), supporting the finding that the enhanced sea ice bottom melting process leads to SIC reduction in EXP. On the other hand, the input of the heat flux is decreased in EXP, which contributes the attenuated sea ice bottom melting (Fig. 6c).

In order to compare the contributions of ice enthalpy and that of heat flux to the increase in *meltb* in EXP quantitatively, we scale the changes in both variables to the same unit by using following equation.

$$\Delta meltb = \frac{F_{EXP}}{q_{EXP}} - \frac{F_{CTL}}{q_{CTL}} = \frac{F_{EXP}\left(\frac{q_{CTL}}{q_{EXP}}\right) - F_{CTL}}{q_{CTL}} \tag{4}$$

where F_{EXP} (F_{CTL}) and q_{EXP} (q_{CTL}) are the net transfer of the energy $F_{cb} - F_{bot}$ and ice enthalpy q in EXP (CTL), respectively. By substituting $F_{EXP} = F_{CTL}$, or $q_{EXP} = q_{CTL}$ into Eq. (4), we can quantify the contribution of q, or F change led by the SIT reduction in unit of cm, as shown in Eq. (5), or (6), respectively.

$$q_{cont} = \left| \frac{F_{CTL}\left(\frac{q_{CTL}}{q_{EXP}} - 1\right)}{q_{CTL}} \right| \tag{5}$$

$$F_{cont} = \left| \frac{F_{EXP} - F_{CTL}}{q_{CTL}} \right| \tag{6}$$

This comparison clearly shows that the augmentation of the ice bottom melting is mainly led by the decrease in the enthalpy rather than the net transfer of the energy ($F_{cb} - F_{bot}$) at the bottom boundary (Fig. 6d).

To further verify that the difference in the strength of the ice bottom melting is caused by the changes in ice enthalpy, sensitivity tests are performed by increasing or decreasing the enthalpy q at all grid points by 30% of its value in CTL. These simulation results verify that the ice bottom melting is amplified (attenuated) by a decrease (increase) in the ice enthalpy q, which

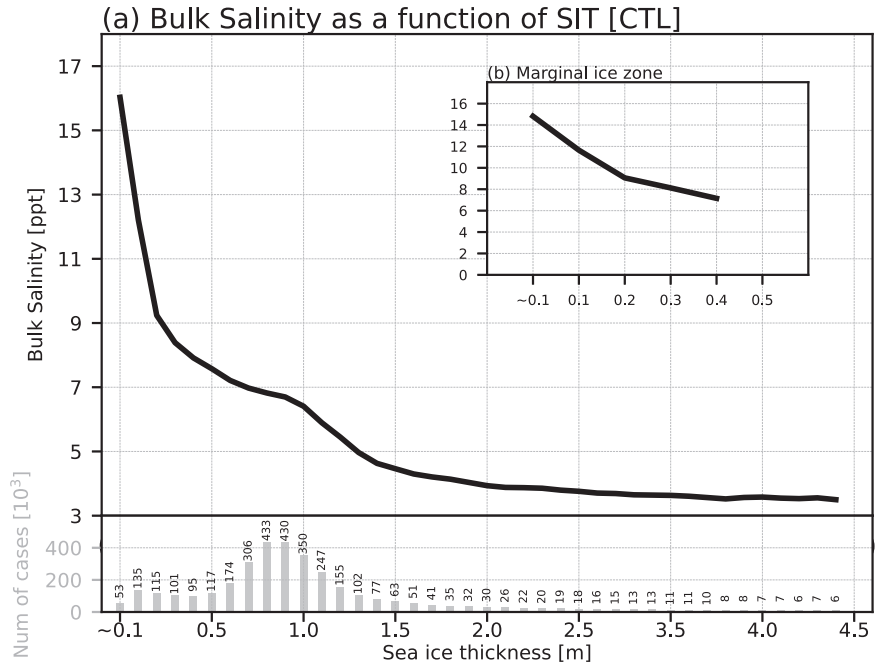

Fig. 7 Relationship between SIT and sea ice bulk salinity (*S*) in simulation. The distribution of ice bulk salinity (ppt) as a function of SIT (m) (upper, black solid line) and the number of cases (lower, gray bars) for Arctic region (**a**) and for MIZ (**b**) in CTL during December 2000–2019.

leads to the decrease (increase) in SIC by -0.72% ($+0.58\%$) (not shown).

The following questions arise: what causes the decrease in the enthalpy q and what is the relationship with the SIT thinning in EXP? The sea ice enthalpy q is the function of the ice bulk salinity (S, ppt) and temperature (T, °C) as follows[60]:

$$q = \rho_i[c_0(T_m - T) + L_0(1 - \frac{T_m}{T}) - c_w T_m] \quad (7)$$

where $\rho_i = 917 \times 10^{-6}$ kg cm^{-3} is the density of ice, T_m is the temperature at which the ice is completely melted ($T_m \equiv -\mu S$), $c_0 = 2,106$ J kg^{-1} °C^{-1} is the specific heat of fresh ice at 0 °C, $c_w = 4,218$ J kg^{-1} °C^{-1} is the specific heat of the ocean, $L_0 = 3.34 \times 10^5$ J kg^{-1} is the latent heat of fusion of fresh ice at 0 °C, and μ is the empirical constant from the relation between the melting temperature and salinity of brine, which is set as 0.054 °C ppt^{-1} following Assur (1958). According to Eq. (7), q weakens when T or S is increased. The amount of energy required to melt a unit volume of sea ice (i.e., q) decreases with increasing ice bulk temperature because the ice easily melts at warm temperatures. As is known, the increase in ice bulk salinity decreases the ice enthalpy by lowering the melting temperature.

Both T and S contribute to the decrease in q in EXP compared to that in CTL. First, the SIT thinning can induce an increase in the ice bulk salinity by weakening the gravity drainage process[61]. Gravity drainage is the dominant desalination process in sea ice, which is the convective exchange of cold and dense brine with fresh sea water[62]. During the formation of new ice, sea ice initially retains the higher amount of the salt presented in the ocean; thus, the sea ice near the surface tends to be more saline than that near the bottom layers. Simultaneously, the upper surface of sea ice is colder than the bottom surface as the atmosphere in this region is colder than the ocean. Therefore, it contains higher salinity as the formation of sea ice with colder temperature results in higher brine salinities. This colder and saltier surface sea ice leads to unstable density stratification. Hence, the brine drains out of the ice and the brine undergoes convective overturning with the ocean, which is replaced by fresh ocean water, and the ice bulk salinity decreases. The thinner the sea ice is, the lower is the drainage strength determined by the extent of density stratification. This is because of a relatively moderate vertical gradient of ice density in thin ice[63,64]. Subsequently, with the thinning of SIT, sea ice undergoes a weak desalination process, which increases the ice bulk salinity[65].

This aforementioned dependency of S on SIT is well simulated in CICE5 by realistically resolving the brine drainage process (Fig. 7). The mean bulk salinity in CTL decreases with increasing SIT, following a negative exponential-like trend over the pan-Arctic region (Fig. 7a). Most of the sea ice has a thickness of fewer than 2.0 m, and bulk salinity is about 4.0 ppt when the ice is 2.0 m but rapidly increased to about 16.5 ppt in the 0.1 m-thick ice. This implies that the reduction in SIT could be a reason for the increase in S, and this relationship is well represented in MIZ (Fig. 7b). The mean S in EXP (6.93ppt) is larger by 0.40ppt than that in CTL (6.53ppt), supporting the fact that the increase in salinity contributes to the decrease in sea ice enthalpy q.

Additionally, the temperature contributes to increasing the ice enthalpy through the albedo-related mechanism. The SIT thinning decreases the ice surface albedo as thin sea ice allows the penetration of more solar radiation into the ice and ocean[66]. Thus, the reduction in SIT leads to ice bulk temperature warming and decreases the ice enthalpy. Fig. 8 shows the time evolution of the Arctic-averaged differences of the ice-albedo (unit of %), the temperature of individual layers of sea ice (unit of °C), and absorption of shortwave heat flux (*Fswabs*, W m^{-2}) between two idealized experiments (i.e., EXP and CTL). Right after the integration starts, the temperature of sea ice began to rise in all layers by SIT reduction in EXP. The degree of increase was stronger in top layers and relatively weaker at bottom layers (Fig. 8b), indicating that the surface process is responsible for this temperature increase. Solar radiation is known to be predominantly absorbed in the uppermost layers of sea ice, with decreasing absorption rates as it penetrates deeper into the ice[67]. Based on the analysis, we can conclude that the primary factor contributing to the increase in sea ice temperature during a decrease in SIT in our experiment is the increased absorption of solar radiation, which means that the warming of the bulk temperature eventually contribute to decrease the sea ice enthalpy q.

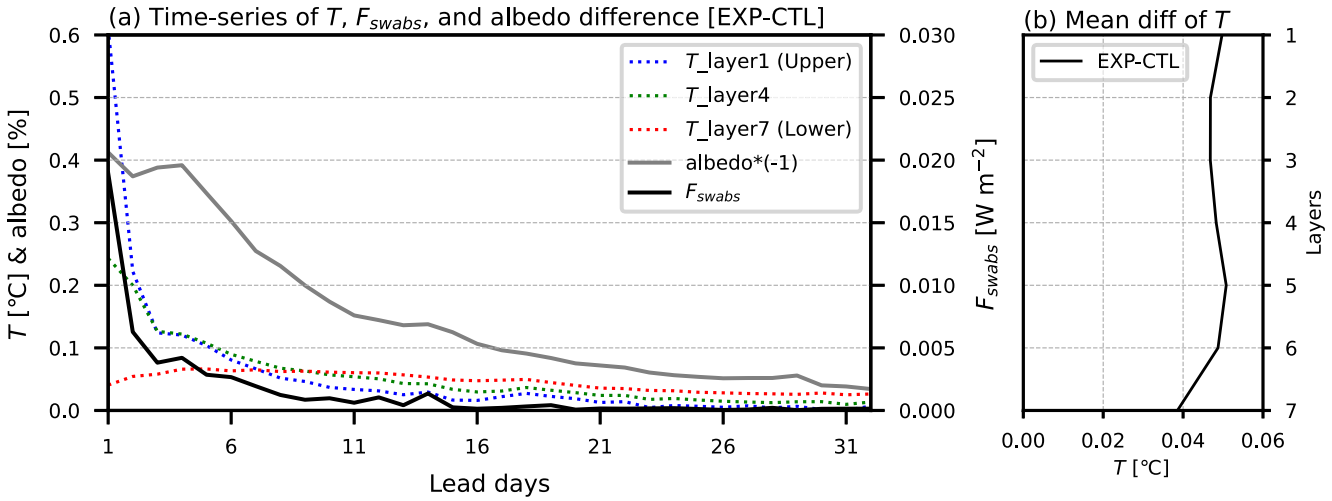

Fig. 8 Changes in sea ice bulk temperature (*T*), albedo, and absorbed shortwave radiation by SIT reduction. The time-series of the differences between EXP and CTL for ice layer temperature (top: blue dotted, middle: green dotted, and bottom: red dotted), ice albedo (gray solid), and absorbed shortwave radiation (black solid) (**a**) and the mean difference in vertical profiles for ice layer temperature between EXP and CTL (**b**) during 2000–2019 in MIZ.

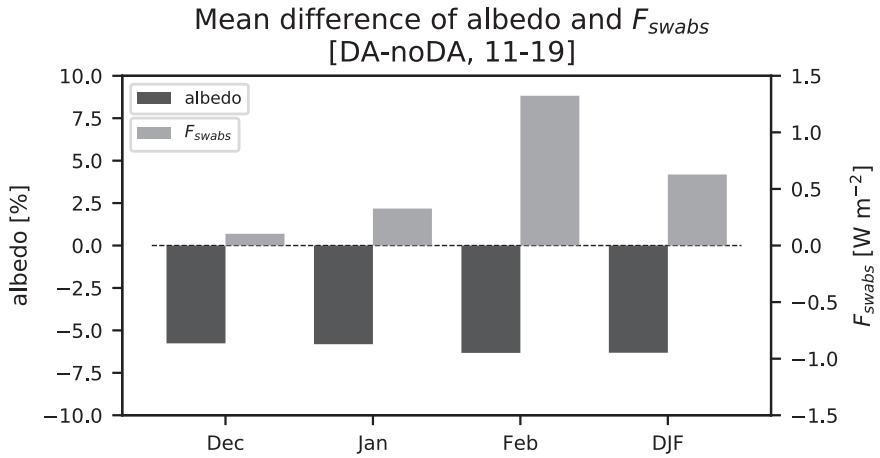

Fig. 9 Impact of SIT data assimilation on albedo and absorbed shortwave radiation during the winter over 2011–2019. The climatological differences in the albedo (black) and absorption of solar radiation (gray) between DA and noDA on December, January, February, and DJF season during 2011–2019 over the regions where the positive biases of SIC are improved by SIT DA.

One might think that the impact of the shortwave would be minimal as time elapses and the dark season approaches, the influence of solar radiation energy diminishes. However, the effects of shortwave radiation become progressively stronger from January to February as the polar night ends in December. While the amount of albedo reduction due to SIT DA remains similar over time, it is evident that the absorption of shortwave radiation gradually augmented as the downward shortwave increases from December to January/February (Fig. 9). This indicates the thinning of SIT due to DA still can increase the absorption of shortwave radiation with reduced albedo during winter season, which in turn contributes to the increase in ice temperature.

DISCUSSION

The DA system was developed to blend the satellite-based SIT data of CS2 and SMOS from the European Space Agency into the CICE5 model using the EnOI method. In addition to SIT, the quality of the SIC reanalysis produced by the SIT DA system was improved for both the boreal summer and winter seasons. The negative and positive SIT biases over the thick and thin sea ice regions in noDA were systematically reduced in the SIT DA experiment due to the complementarity between the SIT satellite data of CS2 and SMOS covering the different major parts of the Arctic regions.

To investigate the detailed physical processes related to SIC reduction to SIT thinning in MIZ during the boreal winter, idealized experiments were performed. The idealized experiment clearly showed the decrease in SIC by SIT thinning and demonstrated that the thermodynamic process is the dominant factor leading to the reduction in SIC. Among various thermodynamic processes, the ice bottom melting process was found to be mainly responsible for the decrease in SIC. Moreover, the decrease in the sea ice enthalpy is the primary driver of augmented ice bottom melting. Ice enthalpy could be attenuated by the increase in ice bulk salinity (temperature) due to the desalination (ice albedo) process with SIT thinning.

Figure 10 is a schematic which summarized our main findings. During the boreal winter, the upper surface of sea ice is colder than the bottom surface due to the colder atmosphere temperatures. The sea ice formed at the top surface has higher brine salinities with colder temperatures, whereas the bottom ice undergoes convective overturning exchange with the fresher ocean water. As a result, unstable density stratification is created, which determines the extent of the brine drained out of the ice by

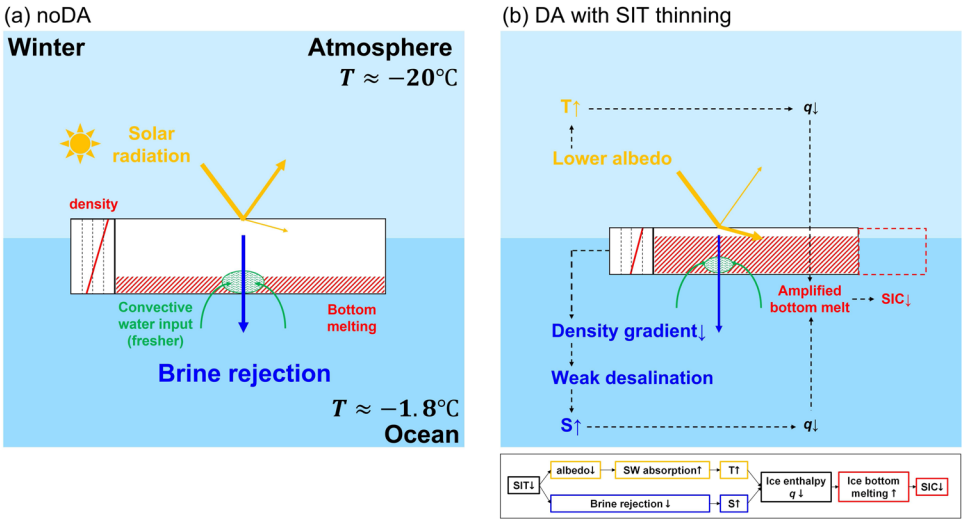

Fig. 10 The thermodynamical process of SIC response to SIT reduction during the boreal winter. A schematic diagram depicting the processes of the response of SIC to the reduction in SIT. The situation in noDA (**a**) and the situation with SIT thinning by DA (**b**) are depicted. The boxes between the atmosphere and the ocean are sea ice. Sketch of downward, reflected and absorbed solar radiation (orange arrows), convective flow of the less salty ocean water (green arrows) freshening the lower part (green circles) within the ice and downward flow of brine into the ocean (blue arrows). The vertical density profile of sea ice is displayed on the left boxes (red lines). The ice bottom melting (i.e., *meltb*) is indicated on the bottom of sea ice (red brushstrokes). The contribution of the ice temperature and salinity is connected the amplification of ice bottom melting through the decrease in enthalpy (black thick dashed lines). In plot (**b**), the box represented by red dashed edge denotes the diminished SIC. The flow diagram below plot (**b**) provides a summary of the involved processes. SW, *T*, and *S* are shortwave, ice bulk temperature, and ice bulk salinity, respectively. The box outline color in the flow diagram is matched to each process in the schematic diagram.

gravity (Fig. 10a). The gravity drainage of brine is the primary reason for the increase in bulk salinity with thinning SIT[61,62,65].

The reduction in SIT leads to the sea ice experiencing less exchange of brine with fresher ocean water, contributing to an increase in salinity and density, especially at the lower layers of the sea ice. In addition, SIT thinning increases the absorption of the solar radiation by reducing the ice surface albedo and acts to elevate the ice bulk temperature[66]. The solar radiation heats the ice in a vertically differentiated manner (i.e., the higher layer, the more heating up)[67], which would contribute to the reduction in density gradient. The resultant lower vertical density gradient due to the SIT reduction weakened the desalination (brine rejection), leading to saltier sea ice (Fig. 10b). The increase in both *T* and *S* leads to the attenuation of ice enthalpy and the resultant amplified melting at the ice bottom contributing the reduction in SIC.

To determine the relative importance of *T* and *S* on *q*, the contributions of *T* and *S* were qualitatively compared as follows:

$$\begin{aligned} T_{cont} &= q(\overline{T_{EXP}}, \overline{S_{CTL}}) - q(\overline{T_{CTL}}, \overline{S_{CTL}}) \\ S_{cont} &= q(\overline{T_{CTL}}, \overline{S_{EXP}}) - q(\overline{T_{CTL}}, \overline{S_{CTL}}) \end{aligned} \quad (8)$$

where T_{cont} and S_{cont} denote the contributions of temperature and salinity on the ice enthalpy change, respectively. The overbar represents the spatial-area-averaged monthly mean. Based on Eq. (8), S_{cont} is roughly 3.4 times larger than T_{cont}, implying that the change in the ice bulk salinity might play a relatively more important role than that in the bulk temperature in the intensification of the ice bottom melting with SIT reduction.

As mentioned above, an obvious physical relation exists between SIC and SIT. This implies that a better understanding of the physical mechanism of the effect of SIT increment on SIC will not only improve our knowledge of the sea ice dynamics but also provide potential factors related to sea ice prediction. In detail, SIT leads to a simultaneous change in SIC, suggesting that the multivariate assimilation using cross-covariance between SIC and SIT might improve the reanalysis quality. This emphasizes the requirement of SIT observations to guarantee the skillful prediction for SIC and SIT.

In this study, the SIC bias in noDA is effectively reduced over thin sea ice regions (i.e., SIT range between 0.2 and 0.4 m) by assimilating the multiple SIT observations (i.e., CS2 and SMOS). It should be noted that the effective range of thickness to reduce the SIC bias may differ from that in a DA framework that assimilates single SIT dataset. For example, the extent of SIC bias reduction in this study would be mainly influenced by SMOS, especially given its effectiveness in thin sea ice regions. However, the impact of CS2 could be also expected, which becomes clear by conducting experiments only with CS2. This implies that distinct impacts of the SIT change on the SIC according to the different SIT dataset is needed to be assessed as a future study.

The study results suggest that the thermodynamic process related to the reduction in SIT might accelerate the decline in sea ice in a warming climate[48]. As emphasized in this study, once SIT thinning leads to SIC reduction, the reduced SIC accelerates the increase in ice bulk temperature via the sea ice albedo feedback, subsequently causing additional SIT thinning. This means that the internal positive feedback between SIC and SIT might lead to Arctic amplification, even without the coupled processes with other climate components.

METHODS

The sea ice model and atmospheric/oceanic forcing

The CICE5 sea ice dynamical model established by the Los Alamos National Laboratory[68] is used in this study. The CICE5 model is a state-of-the-art sea ice model with complex physical parameterization schemes and is utilized as a sea ice component of the National Center for Atmospheric Research Community Earth System Model[69,70]. CICE5 model classifies the ice thickness distribution into five categories. To resolve the sea ice temperature and salinity variations, the individual SIT categories comprise seven vertical ice layers and one snow layer. The thermodynamic and dynamic processes of the model are mushy layer thermodynamics and

elastic-anisotropic-plastic dynamics, respectively[61,71]. Additionally, the model comprises recent complex physics, such as level-ice formulation scheme for melt pond parameterization[72] and a mechanical redistribution scheme for ridging parameterization[73]. The model domain covers all longitudes and the latitudes poleward to 89.71°N. The horizontal resolution is approximately 1° with 320 × 384 dimension on a displaced pole grid, and the time step of the model is set to 1 h.

Atmospheric boundary conditions, such as the surface momentum (i.e., zonal and meridional wind stresses) and the surface heat fluxes (i.e., incoming and outgoing longwave and shortwave radiations), for the CICE5 are obtained from the NCEP-DOE 2 Reanalysis dataset[74]. Moreover, the modeled sea surface temperature (SST) from the National Oceanic and Atmospheric Administration[75] is input to the Optimal Interpolation SST version 2 with the restoring time scale of 20 days.

Data assimilation scheme

The satellite-derived SIT observations are assimilated into the CICE5 model using an EnOI scheme with a 1-day assimilation cycle[52,53,76–78]. The EnOI scheme approximates the background error covariance matrix using a stationary ensemble member. If the available computational resources are limited, the EnOI provides a cost-effective alternative to the ensemble Kalman filter[79]. Stationary ensemble members (i.e., background error perturbations) for the EnOI are generated following a methodology similar to that for obtaining bred vectors[54]. To consider the seasonal differences in the spatial distribution of the perturbations, the background error covariance matrix on any particular day is calculated using the background perturbations on a corresponding day from 1982 to 2019. Consequently, the background error covariance matrix has a seasonal cycle, and the total number of samples for formulating the background error covariance matrix on any given day is 38 (i.e., one sample per year). For further details on the equations and schematic, refer to previous study[54].

Sea ice data for data assimilation and validation

The satellite-observed SIT data used for the assimilation experiment are derived from the CS2 and SMOS datasets. Among the various products from CS2, radar altimeter-based Level-4 SIT data retrieved by assuming hydrostatic balance and nominal densities of snow, ice, and water of sea ice freeboard are used. The SIT is retrieved only for the grid point whose area with the SIC exceeds 70% of the total area (i.e., SIC > 0.7)[29,80]. Considering that CS2 is specialized for the regions of the filled sea ice, the CS2 data is assimilated for the region where the sea ice is thicker than 1.0 m[81].

The Level-3 SMOS daily SIT data versions 3.1 (for ~2018) and 3.2 (for 2019) are used for sea ice thinner than 1.0 m[30,81–83]. The SMOS SIT data are obtained from the brightness temperature using a single-layer emissivity model. Due to the saturation of the brightness temperature with SIT, thin sea ice in SMOS has small uncertainties and thick sea ice is strongly underestimated[30,82,83].

The CS2 (SMOS) data are on the polar-stereographic grid system and have a horizontal resolution of 25 (12.5) km. Both SIT products are utilized for assimilation during 2011–2019. The uncertainties of the SIT data are 1.5 m (0.3 m for random + 1.2 m for systematic) for CS2 and 0.7 m for SMOS[42]. The satellite-based SIT observations are only available for the cold season from October to April, signifying that observed data from May to September are not assimilated.

To validate the modeled SIC, the Climate Data Record (CDR) of the satellite-based daily SIC is used; it was retrieved using passive microwave data[84]. Additionally, the Pan-Arctic Ice-Ocean Modeling and Assimilation System (PIOMAS) SIC and SIT are used for the validation[85]. For evaluation, the model output and the satellite observation are re-gridded onto the 1° rectilinear latitude/longitude grid system from the original grid system.

DATA AVAILABILITY

The satellite data set of daily sea ice thickness from CryoSat-2 Level-4 Sea Ice Elevation, Freeboard, and Thickness, Version 1 (http://nsidc.org/data/RDEFT4) and SMOS Level-3 product (https://smos-diss.eo.esa.int/oads/access/collection/L3_SIT_Open) are provided by the European Space Agency. The Climate Data Record of Passive Microwave sea ice concentration version 4 data is provided by National Snow and Ice Data Center (http://nsidc.org/data/G02202). The reanalysed sea ice concentration and thickness from PIOMAS are provided by Polar Science Center (http://psc.apl.uw.edu/research/projects/arctic-sea-ice-volume-anomaly/). The prescribed atmospheric/oceanic data as the boundary condition to run CICE5 from NCEP-DOE Reanasis 2 with Global T62 Gaussian grid (https://psl.noaa.gov/data/gridded/data.ncep.reanalysis2.html) and OISST version 2 high resoluation dataset with 0.25 degree latitude/longitude global grid (https://psl.noaa.gov/data/gridded/data.noaa.oisst.v2.highres.html) are provided by the National Oceanic and Atmospheric Administration. All simulated data detailed in this manuscript is available upon reasonable request by the authors.

CODE AVAILABILITY

EnOI-based DA system is available via https://github.com/jglee-cnu/CICE5_DA_EnOI_SIT.git.

Received: 12 December 2022; Accepted: 14 June 2023;
Published online: 24 June 2023

REFERENCES

1. Kwok, R. & Rothrock, D. A. Decline in Arctic sea ice thickness from submarine and ICESat records: 1958-2008. *Geophys. Res. Lett.* **36**, 1–5 (2009).
2. Serreze, M. C., Barrett, A. P., Stroeve, J. C., Kindig, D. N. & Holland, M. M. The emergence of surface-based Arctic amplification. *Cryosphere* **3**, 11–19 (2009).
3. Stroeve, J. C. et al. Trends in Arctic sea ice extent from CMIP5, CMIP3 and observations. *Geophys Res. Lett.* **39**, 1–7 (2012).
4. Meier, W. N. et al. Sea Ice. 1–9 (2021).
5. Goosse, H., Arzel, O., Bitz, C. M., de Montety, A. & Vancoppenolle, M. Increased variability of the Arctic summer ice extent in a warmer climate. *Geophys Res Lett.* **36**, 1–5 (2009).
6. Holland, M. M., Bitz, C. M., Tremblay, L. B. & Bailey, D. A. The role of natural versus forced change in future rapid summer arctic ice loss. *Geophys Monogr. Ser.* **180**, 133–150 (2008).
7. Massonnet, F. et al. Arctic sea-ice change tied to its mean state through thermodynamic processes. *Nat. Clim. Chang* **8**, 599–603 (2018).
8. Liu, M. & Kronbak, J. The potential economic viability of using the Northern Sea Route (NSR) as an alternative route between Asia and Europe. *J. Transp. Geogr.* **18**, 434–444 (2010).
9. Smith, L. C. & Stephenson, S. R. New Trans-Arctic shipping routes navigable by midcentury. *Proc. Natl Acad. Sci.* **110**, 6–10 (2013).
10. Bader, J. et al. A review on Northern Hemisphere sea-ice, storminess and the North Atlantic Oscillation: Observations and projected changes. *Atmos. Res.* **101**, 809–834 (2011).
11. Kennel, C. F. & Yulaeva, E. Influence of Arctic sea-ice variability on Pacific trade winds. *Proc. Natl Acad. Sci.* **117**, 2824–2834 (2020).
12. Meredith, M. et al. Polar regions. In H.-O Pörtner, et al. (Eds.). *IPCC Special Report on the Ocean and Cryosphere in a Changing Climate* 203–320 (2019).
13. Pedersen, R. A., Cvijanovic, I., Langen, P. L. & Vinther, B. M. The impact of regional Arctic sea ice loss on atmospheric circulation and the NAO. *J. Clim.* **29**, 889–902 (2016).
14. Eicken, H. Ocean science: Arctic sea ice needs better forecasts. *Nature* **497**, 431–433 (2013).
15. Chevallier, M., Mélia, D. S. Y., Voldoire, A., Déqué, M. & Garric, G. Seasonal forecasts of the pan-arctic sea ice extent using a GCM-based seasonal prediction system. *J. Clim.* **26**, 6092–6104 (2013).
16. Wang, W., Chen, M. & Kumar, A. Seasonal prediction of arctic sea ice extent from a coupled dynamical forecast system. *Mon. Weather Rev.* **141**, 1375–1394 (2013).
17. Lisæter, K. L., Rosanova, J. & Evensen, G. Assimilation of ice concentration in a coupled ice-ocean model, using the Ensemble Kalman filter. *Ocean Dyn.* **53**, 368–388 (2003).
18. Liu, X., Sha, Z. & Lu, C. Cice-letkf ensemble analysis system with application to arctic sea ice initialization. *J. Mar. Sci. Eng.* **9**, 920 (2021).
19. Caya, A., Buehner, M. & Carrieres, T. Analysis and forecasting of sea ice conditions with three-dimensional variational data assimilation and a coupled ice-ocean model. *J. Atmos. Ocean Technol.* **27**, 353–369 (2010).
20. Lindsay, R. W. & Zhang, J. Assimilation of ice concentration in an ice-ocean model. *J. Atmos. Ocean Technol.* **23**, 742–749 (2006).

21. Massonnet, F. et al. A model reconstruction of the Antarctic sea ice thickness and volume changes over 1980-2008 using data assimilation. *Ocean Model (Oxf.)* **64**, 67–75 (2013).
22. Stark, J. D., Ridley, J., Martin, M. & Hines, A. Sea ice concentration and motion assimilation in a sea ice-ocean model. *J. Geophys. Res. Oceans* **113**, 1–19 (2008).
23. Blanchard-Wrigglesworth, E., Armour, K. C., Bitz, C. M. & Deweaver, E. Persistence and inherent predictability of arctic sea ice in a GCM ensemble and observations. *J. Clim.* **24**, 231–250 (2011).
24. Guemas, V. et al. A review on Arctic sea-ice predictability and prediction on seasonal to decadal time-scales. *Q J. R. Meteorol. Soc.* **142**, 546–561 (2016).
25. Laxon, S., Peacock, H. & Smith, D. High interannual variability of sea ice thickness in the Arctic region. *Nature* **425**, 947–950 (2003).
26. Massonnet, F., Fichefet, T. & Goosse, H. Prospects for improved seasonal Arctic sea ice predictions from multivariate data assimilation. *Ocean Model (Oxf.)* **88**, 16–25 (2015).
27. Day, J. J., Hawkins, E. & Tietsche, S. Will Arctic sea ice thickness initialization improve seasonal forecast skill? *Geophys Res Lett.* **41**, 7566–7575 (2014).
28. Day, J. J., Tietsche, S. & Hawkins, E. Pan-arctic and regional sea ice predictability: Initialization month dependence. *J. Clim.* **27**, 4371–4390 (2014).
29. Kurtz, N. & Harbeck, J. CryoSat-2 Level-4 Sea Ice Elevation, Freeboard, and Thickness, Version 1. *Boulder, Colorado USA. NASA National Snow and Ice Data Center Distributed Active Archive Center*. 0–9 (2017).
30. Tian-Kunze, X. et al. SMOS-derived thin sea ice thickness: Algorithm baseline, product specifications and initial verification. *Cryosphere* **8**, 997–1018 (2014).
31. Allard, R. et al. Analyzing the impact of CryoSat-2 ice thickness initialization on seasonal Arctic Sea Ice prediction. *Ann. Glaciol.* **61**, 78–85 (2020).
32. Blockley, E. W. & Peterson, Andrew K. Improving Met Office seasonal predictions of Arctic sea ice using assimilation of CryoSat-2 thickness. *Cryosphere* **12**, 3419–3438 (2018).
33. Fiedler, E. K. et al. Assimilation of sea ice thickness derived from CryoSat-2 along-track freeboard measurements into the Met Office's Forecast Ocean Assimilation Model (FOAM). *Cryosphere* **16**, 61–85 (2022).
34. Mignac, D., Martin, M., Fiedler, E., Blockley, E. & Fournier, N. Improving the Met Office's Forecast Ocean Assimilation Model (FOAM) with the assimilation of satellite-derived sea-ice thickness data from CryoSat-2 and SMOS in the Arctic. *Q. J. R. Meteorological Soc.* **148**, 1144–1167 (2022).
35. Mu, L. et al. Improving sea ice thickness estimates by assimilating CryoSat-2 and SMOS sea ice thickness data simultaneously. *Q. J. R. Meteorological Soc.* **144**, 529–538 (2018).
36. Yang, Q. et al. Improving Arctic sea ice seasonal outlook by ensemble prediction using an ice-ocean model. *Atmos. Res.* **227**, 14–23 (2019).
37. Xie, J., Counillon, F. & Bertino, L. Impact of assimilating a merged sea-ice thickness from CryoSat-2 and SMOS in the Arctic reanalysis. *Cryosphere* **12**, 3671–3691 (2018).
38. Bertino, L., Lisæter, K. A. & Scient, S. The TOPAZ monitoring and prediction system for the Atlantic and Arctic Oceans. *J. Oper. Oceanogr.* **1**, 15–18 (2008).
39. Gupta, M., Caya, A. & Buehner, M. Assimilation of SMOS sea ice thickness in the regional ice prediction system. *Int. J. Remote Sens* **42**, 4583–4606 (2021).
40. Xie, J., Counillon, F., Bertino, L., Tian-Kunze, X. & Kaleschke, L. Benefits of assimilating thin sea ice thickness from SMOS into the TOPAZ system. *Cryosphere* **10**, 2745–2761 (2016).
41. Yang, Q. et al. Assimilating SMOS sea ice thickness into a coupled ice-ocean model using a local SEIK filter. *J. Geophys. Res. Oceans* **119**, 6680–6692 (2014).
42. Chen, Z., Liu, J., Song, M., Yang, Q. & Xu, S. Impacts of assimilating satellite sea ice concentration and thickness on Arctic sea ice prediction in the NCEP climate forecast system. *J. Clim.* **30**, 8429–8446 (2017).
43. Fritzner, S., Graversen, R., Christensen, K., Rostosky, P. & Wang, K. Impact of assimilating sea ice concentration, sea ice thickness and snow depth in a coupled ocean-sea ice modelling system. *Cryosphere* **13**, 491–509 (2019).
44. Mu, L. et al. Arctic-Wide Sea Ice Thickness Estimates From Combining Satellite Remote Sensing Data and a Dynamic Ice-Ocean Model with Data Assimilation During the CryoSat-2 Period. *J. Geophys. Res. Oceans* **123**, 7763–7780 (2018).
45. Liang, X., Zhao, F., Li, C., Zhang, L. & Li, B. Evaluation of arciops sea ice forecasting products during the ninth chinare-arctic in summer 2018. *Adv. Polar Sci.* **31**, 14–25 (2020).
46. Labe, Z., Peings, Y. & Magnusdottir, G. Contributions of Ice Thickness to the Atmospheric Response From Projected Arctic Sea Ice Loss. *Geophys Res Lett.* **45**, 5635–5642 (2018).
47. Serreze, M. C. & Barry, R. G. Processes and impacts of Arctic amplification: A research synthesis. *Glob. Planet Change* **77**, 85–96 (2011).
48. Lang, A., Yang, S. & Kaas, E. Sea ice thickness and recent Arctic warming. *Geophys. Res. Lett.* **44**, 409–418 (2017).
49. Holland, M. M., Bailey, D. A. & Vavrus, S. Inherent sea ice predictability in the rapidly changing Arctic environment of the Community Climate System Model, version 3. *Clim. Dyn.* **36**, 1239–1253 (2011).
50. Overland, J. E. & Wang, M. Recent extreme arctic temperatures are due to a split polar vortex. *J. Clim.* **29**, 5609–5616 (2016).
51. Semmler, T., Jung, T. & Serrar, S. Fast atmospheric response to a sudden thinning of Arctic sea ice. *Clim. Dyn.* **46**, 1015–1025 (2016).
52. Kaurkin, M. N., Ibrayev, R. A. & Belyaev, K. P. ARGO data assimilation into the ocean dynamics model with high spatial resolution using Ensemble Optimal Interpolation (EnOI). *Oceanol. (Wash. D. C.)* **56**, 774–781 (2016).
53. Mignac, D., Tanajura, C. A. S., Santana, A. N., Lima, L. N. & Xie, J. Argo data assimilation into HYCOM with an EnOI method in the Atlantic Ocean. *Ocean Sci.* **11**, 195–213 (2015).
54. Lee, J. G. & Ham, Y. G. Satellite-Based Data Assimilation System for the Initialization of Arctic Sea Ice Concentration and Thickness Using CICE5. *Front Clim.* **4**, 797733 (2022).
55. Koenigk, T. & Mikolajewicz, U. Seasonal to interannual climate predictability in mid and high northern latitudes in a global coupled model. *Clim. Dyn.* **32**, 783–798 (2009).
56. Chevallier, M. & Salas-Mélia, D. The role of sea ice thickness distribution in the arctic sea ice potential predictability: A diagnostic approach with a coupled GCM. *J. Clim.* **25**, 3025–3038 (2012).
57. Bi, H. et al. Estimating sea-ice volume flux out of the Laptev Sea using multiple satellite observations. *Polar Res.* **35**, 24875 (2016).
58. Ivanova, D. P., McClean, J. L. & Hunke, E. C. Interaction of ocean temperature advection, surface heat fluxes and sea ice in the marginal ice zone during the North Atlantic Oscillation in the 1990s: A modeling study. *J. Geophys. Res. Oceans* **117**, C02031 (2012).
59. Martin, T. Arctic Sea Ice Dynamics: Drift and Ridging in Numerical Models and Observations. PhD thesis, Alfred Wegener Inst. for Polar and Marine Res. *Universität Bremen* (2007).
60. Bitz, C. M. & Lipscomb, W. H. An energy-conserving thermodynamic model of sea ice. *J. Geophys. Res. Oceans* **104**, 15669–15677 (1999).
61. Turner, A. K., Hunke, E. C. & Bitz, C. M. Two modes of sea-ice gravity drainage: A parameterization for large-scale modeling. *J. Geophys. Res. Oceans* **118**, 2279–2294 (2013).
62. Notz, D. & Worster, M. G. Desalination processes of sea ice revisited. *J. Geophys. Res. Oceans* **114**, C05006 (2009).
63. Notz, D. & Grae Worster, M. In situ measurements of the evolution of young sea ice. *J. Geophys. Res. Oceans* **113**, C03001 (2008).
64. Wells, A. J., Wettlaufer, J. S. & Orszag, S. A. Maximal potential energy transport: A variational principle for solidification problems. *Phys. Rev. Lett.* **105**, 254502 (2010).
65. Kovacs, A. Sea Ice Part I. Bulk Salinity Versus Ice Floe Thickness. CRREL Rep. 96-7, U.S. Army Cold Regions Research and Engineering Laboratory (1996).
66. Briegleb, B. P. & Light, B. A Delta-Eddington Multiple Scattering Parameterization for Solar Radiation in the Sea Ice Component of the Community Climate System Model. Tech. rep., Boulder, CO (2007).
67. Lu, P., Cheng, B., Leppäranta, M. & Li, Z. Partitioning of solar radiation in Arctic sea ice during melt season. *Oceanologia* **60**, 464–477 (2018).
68. Hunke, E. C., Lipscomb, W. H., Turner, A. K., Jeffery, N. & Elliott, S. CICE: the Los Alamos Sea Ice Model Documentation and Software User's Manual Version 5.1. LA-CC-06-012. (2015).
69. Danabasoglu, G. et al. The Community Earth System Model Version 2 (CESM2). *J. Adv. Model Earth Syst.* **12**, 1–35 (2020).
70. Hurrell, J. W. et al. The community earth system model: A framework for collaborative research. *Bull. Am. Meteorol. Soc.* **94**, 1339–1360 (2013).
71. Wilchinsky, A. V. & Feltham, D. L. Modelling the rheology of sea ice as a collection of diamond-shaped floes. *J. Nonnewton Fluid Mech.* **138**, 22–32 (2006).
72. Hunke, E. C., Hebert, D. A. & Lecomte, O. Level-ice melt ponds in the Los Alamos sea ice model, CICE. *Ocean Model (Oxf.)* **71**, 26–42 (2013).
73. Lipscomb, W. H., Hunke, E. C., Maslowski, W. & Jakacki, J. Ridging, strength, and stability in high-resolution sea ice models. *J. Geophys Res Oceans* **112**, C03S91 (2007).
74. Kanamitsu, M. et al. NCEP–DOE AMIP-II Reanalysis (R-2). *Bull. Am. Meteorol. Soc.* **83**, 1631–1644 (2002).
75. Reynolds, R. W., Rayner, N. A., Smith, T. M., Stokes, D. C. & Wang, W. An improved in situ and satellite SST analysis for climate. *J. Clim.* **15**, 1609–1625 (2002).
76. Backeberg, B. C., Counillon, F., Johannessen, J. A. & Pujol, M. I. Assimilating along-track sla data using the EnOI in an eddy resolving model of the agulhas system. *Ocean Dyn.* **64**, 1121–1136 (2014).
77. Kim, Y. H., Hwang, C. & Choi, B. J. An assessment of ocean climate reanalysis by the data assimilation system of KIOST from 1947 to 2012. *Ocean Model (Oxf.)* **91**, 1–22 (2015).
78. Zhou, W., Li, J., Xu, F., Shu, Y. & Feng, Y. The impact of ocean data assimilation on seasonal predictions based on the National Climate Center climate system model. *Acta Oceanologica Sin.* **40**, 58–70 (2021).
79. Oke, P. R., Sakov, P. & Corney, S. P. Impacts of localisation in the EnKF and EnOI: Experiments with a small model. *Ocean Dyn.* **57**, 32–45 (2007).

80. Kurtz, N. T., Galin, N. & Studinger, M. An improved CryoSat-2 sea ice freeboard retrieval algorithm through the use of waveform fitting. *Cryosphere* **8**, 1217–1237 (2014).
81. Ricker, R. et al. A Weekly Arctic Sea-Ice Thickness Data Record from merged CryoSat-2 and SMOS Satellite Data. *The Cryosphere Discussions* 1–27 https://doi.org/10.5194/tc-2017-4 (2017)
82. Kaleschke, L., Tian-Kunze, X., Maaß, N., Mäkynen, M. & Drusch, M. Sea ice thickness retrieval from SMOS brightness temperatures during the Arctic freeze-up period. *Geophys Res Lett.* **39**, 1–5 (2012).
83. Kaleschke, L. et al. SMOS sea ice product: Operational application and validation in the Barents Sea marginal ice zone. *Remote Sens Environ.* **180**, 264–273 (2016).
84. Meier, W. N. et al. NOAA/NSIDC Climate Data Record of Passive Microwave Sea Ice Concentration, Version 3. (2017).
85. Zhang, J. & Rothrock, D. A. Modeling global sea ice with a thickness and enthalpy distribution model in generalized curvilinear coordinates. *Mon. Weather Rev.* **131**, 845–861 (2003).

ACKNOWLEDGEMENTS

This study was supported by the Korea Meteorological Administration Research and Development Program under Grant KMI2021–01210. Y.-G.H. was supported by Korea Environmental Industry & Technology Institute (KEITI) through "Project for developing an observation-based GHG emissions geospatial information map", funded by Korea Ministry of Environment (MOE) (RS-2023-00232066).

AUTHOR CONTRIBUTIONS

J.-G.L. and Y.-G.H. designed the research and wrote the paper. J.-G.L. performed the experiments and analysed the data. All authors discussed the methodology, results and structure of the paper.

COMPETING INTERESTS

The authors declare no competing interests.

ADDITIONAL INFORMATION

Correspondence and requests for materials should be addressed to Yoo-Geun Ham.

Reprints and permission information is available at http://www.nature.com/reprints

Publisher's note Springer Nature remains neutral with regard to jurisdictional claims in published maps and institutional affiliations.